An analytical model for wind-driven Arctic summer sea ice drift

H.-S. Park[1] and A. L. Stewart[2]

[1]{Korea Institute of Geoscience and Mineral Resources, Daejeon, South Korea}

[2]{Department of Atmospheric and Oceanic Sciences, University of California, Los Angeles}

Correspondence to: H.-S. Park (hspark1@gmail.com)

Abstract

The authors present an analytical model for wind-driven free drift of sea ice that allows for an arbitrary mixture of ice and open water. The model includes an ice-ocean boundary layer with an Ekman spiral, forced by transfers of wind-input momentum both through the sea ice and directly into the open water between the ice floes. The analytical tractability of this model allows efficient calculation of the ice velocity provided that the surface wind field is known and that the ocean geostrophic velocity is relatively weak. The model predicts that variations in the ice thickness or concentration should substantially modify the rotation of the velocity between the 10m winds, the sea ice, and the ocean.

The model is evaluated against recent observational data from the first ice-tethered profiler equipped with a velocity sensor (ITP-V). Though these observations were made in winter when internal stresses in the ice are likely to have been dynamically significant, our model is largely able to capture the dependence of the ice speed and the wind/ice/ocean turning angles on the wind speed. The model is then used to show that strengthening of the southerlies on intraseasonal time scales (around 1 week) reduces summer sea ice concentration in the Pacific sector via wind-induced sea ice drift. The 10m winds from ERA-Interim reanalysis are used to model the sea ice drift induced by 27 southerly intensification events between 1990 and 2012. The resulting anomalous changes in sea ice concentration are calculated and found to compare closely with satellite observations.

1 Introduction

The drift of Arctic sea ice is largely explained by surface winds and upper-ocean currents. The effect of the mean geostrophic upper-ocean currents on the average circulation of sea ice pack is known to be as important as the mean wind field (Thorndike and Colony, 1982). However, the role of the winds becomes increasingly important over shorter time scales: On time scales from days to months, surface wind variability explains more than 70% of the sea ice motion (Thorndike and Colony, 1982), and is well correlated with the surface ocean velocity (Cole et al., 2014). The synoptic eddy surface winds result in a primary mode of upper-ocean velocity variability with a period of 2–5 days over the ice-covered Arctic Ocean (Plueddemann et al., 1998). The tight connection between surface winds and upper ocean velocity over ice-covered Arctic Ocean suggests that resolving the wind-induced surface Ekman flow is essential for simulating sea ice motions.

Many simple sea ice models assume steady ocean currents and prescribe a quadratic relationship with an empirically-chosen turning angle between the ice stress and surface ocean velocity (Hibler 1979; Thorndike and Colony, 1982; Bitz et al., 2002; Liu et al., 2011; Uotila et al., 2012). This model configuration has limitations in simulating wind-induced sea ice drift on intraseasonal time scales, during which time-varying Ekman layer flows in the ice-ocean boundary layer (IOBL) may be important. The effect of the surface Ekman flow on sea ice motion can be resolved by coupling the sea ice model to a comprehensive ocean model (Zhang and Rothrock, 2003; Uotila et al., 2012). However, such an approach is computationally expensive, and makes it difficult to disentangle the physical processes controlling sea ice drift.

In the past few decades, considerable advances have been made in understanding the physics of the IOBL, notably via the development of Rossby similarity theory (McPhee, 1979; 1981; 1994; 2008). In the case of an unstratified surface layer, this theory connects the ocean's Ekman layer to the ice base via a thin surface layer in which the velocity shear follows the *law of the wall* and the vertical eddy viscosity varies linearly to zero. In contrast to frequently-used quadratic drag parameterizations (e.g. Hibler 1979; Thorndike and Colony, 1982), this results in a quadratic drag coefficient and turning angle that depend on the stress velocity and the hydraulic roughness length of the ice base. However, the assumptions underlying Rossby similarity theory make it inapplicable to the case of a mixture of sea ice

and open water, which is typical of the Arctic in summer.

In Sec. 2 we derive an approximate analytical model for wind-induced sea ice drift that accounts for the Ekman spiral in the IOBL and allows for an arbitrary mixture of ice and water, but neglects internal stress within the ice. The model is therefore most appropriate to the marginal ice zone which covers much of the Arctic during summer. This approach has both theoretical and practical merits: because the Ekman layer is resolved in the momentum balance, the turning angle is a prognostic variable in our model, allowing us to explore the dependence of both the ice drift speed and the wind/ice/ocean turning angles on the concentration and thickness of the sea ice. The analytical tractability of the model allows efficient calculation of the sea ice drift, certainly much more so than running a full coupled model of the Arctic. We exploit this efficiency to compare our model's predictions against observations of Arctic sea ice concentration and velocity: the data sources and reanalysis products used for this purpose are described in Sec. 3.

In Sec. 4, we evaluate our model against recent observations from an ice-tethered profiler (Cole et al., 2014), focusing on the angles between the wind and ice velocities and between the ice and ocean velocities. At face value our model may not appear to be applicable to this data because the measurements were made in the Beaufort Sea in winter, when the sea ice concentration is close to 100% and internal stress is likely to be dynamically significant (Leppäranta, 2005). However, the analysis of Cole et al. (2014) suggests that the ice floe velocity was in fact close to a free drift regime, and that the vertical buoyancy flux in the IOBL was small, compared to previous winter observations (see *e.g.* McPhee, 2008). Consequently our model is largely captures the dependence of the ice speed and turning angle on the surface wind speed.

In Sec. 5 we apply our model to predict the anomalous change in Arctic sea ice concentration associated with intraseasonal intensification of the southerly winds in the Pacific sector. This serves a dual purpose: First, it is a test of our model's assumptions that the summer sea ice drift can be described accurately by neglecting internal stresses and assuming constant drag coefficients at the ice-ocean, atmosphere-ice, and atmosphere-ocean interfaces. Second, by extension, it tests the hypothesis that the anomalous reduction in sea ice concentration in the Pacific sector during southerly wind events can be attributed to the mechanical effect of

3

wind-driven ice drift, rather than thermodynamic effects. Many previous observational analyses provided only statistical connections between the southerly winds and sea ice cover. For example, the strength of south-westerlies over the Barents Sea is well correlated with sea ice cover in winter (Sorteberg and Kvingedal, 2006; Liptak and Strong, 2014) and the development of anomalous southerlies over the Pacific sector of the Arctic is often followed by a reduction of sea ice cover in the spring and summer (Wu et al., 2006; Serreze et al., 2003). We demonstrate that the southerly wind-induced sea ice advection, accelerated by wind-induced surface Ekman flow, can substantially decrease sea ice concentration over a time scale of one week.

2 An analytical model for wind-driven sea ice motion

In this section we employ a simplified sea ice model to obtain analytical expressions for the sea ice velocity as a function of surface wind speed. In Sec. 2.1 we formulate an approximate sea ice momentum balance appropriate for basin-scale motions, and then in Sec. 2.2 we derive an analytical solution for the sea ice velocity, assuming that the surface wind speed is known.

2.1 Model formulation

We employ a "mixture layer" model of Arctic sea ice (Gray and Morland, 1994), which describes the evolution of ice floes interspersed with patches of open water. The thickness-integrated momentum balance for such a mixture layer may be written as (Heorton et al., 2014),

$$\rho_i h_i \frac{D\vec{u}_i}{Dt} = \varphi(\vec{\tau}_{ai} - \vec{\tau}_{io}) - \rho_i h_i f(\hat{Z} \times \vec{u}_i) - \rho_i h_i g \nabla \eta + \nabla \cdot \boldsymbol{\sigma}. \tag{1}$$

where h_i is the ice thickness, ρ_i is the ice density, $\vec{u}_i$ is the ice velocity vector, η is the sea surface height, φ is the sea ice fraction, f is the Coriolis parameter, g is the acceleration due to gravity, and $\hat{Z}$ is a vertical unit vector. Equation (1) states that the ice/water mixture layer is accelerated by momentum exchanges between the ice and the atmosphere ($\vec{\tau}_{ai}$) and between the ice and the ocean ($\vec{\tau}_{io}$), by the Coriolis force, by horizontal pressure variations due to sea surface tilt, and by the divergence of a stress tensor ($\boldsymbol{\sigma}$) representing internal stress in the ice.

1   We first write the lateral pressure gradient term in terms of the ocean near-surface geostrophic

2   velocity $\vec{u}_g$,

$$f\hat{Z} \times \vec{u}_g = \rho_i h_i g \nabla \eta. \tag{2}$$

3   We are concerned with sea ice evolution over a typical time scale 1 week with a velocity

4   scale of around 0.2 m/s, implying a length scale of around 100 km. The ice acceleration term

5   in (1) may therefore be safely neglected (McPhee 1980; Thorndike and Colony, 1982). This

6   precludes the sea ice undergoing inertial oscillations, though the diameter of such oscillations

7   would only be a few km at most, much smaller than the drift length scale of 100 km. In

8   summer, the Arctic sea ice concentration is mostly below 80% (see Fig. 1), so away from

9   coastal shear margins the internal friction term in (1) is also negligible (Leppäranta, 2005;

10 Kawaguchi and Mitsudera, 2008). This simplifies the momentum balance to

$$\rho_i h_i f\hat{Z} \times \left(\vec{u}_i - \vec{u}_g\right) = \varphi(\vec{\tau}_{ai} - \vec{\tau}_{io}), \tag{3}$$

11 Similar scaling arguments suggest that the pressure gradient due to the sea surface tilt may

12 also be negligible. For now we retain this term because it is analytically tractable, but in Secs.

13 4 and 5 below, we will neglect the geostrophic ocean velocity term in (3).

14 Equation (3) states that the shear between the mixture layer and the ocean's surface

15 geostrophic velocity, or equivalently the total shear across the ice-ocean boundary layer

16 (IOBL; McPhee, 2012) lies perpendicular to the vertical stress divergence in the sea ice. This

17 equation does not account for momentum imparted from the winds to the water between the

18 ice floes in the mixture layer, which is assumed to be transferred directly to the ocean below

19 (Gray and Morland, 1994). The total stress felt by the ocean at the base of the mixture layer is

20 therefore

$$\vec{\tau}_o = (1 - \varphi)\vec{\tau}_{ao} + \varphi\vec{\tau}_{io}, \tag{4}$$

21 where $\vec{\tau}_{ao}$ is the momentum imparted to the ocean from the atmosphere between the sea ice

22 floes. We adopt an approach similar to Rossby similarity theory for the IOBL, assuming that

23 the ocean velocity follows an Ekman spiral beneath the mixture layer (McPhee, 2012). The

24 ocean velocity at the top of the Ekman layer is therefore given as

$$\vec{u}_o - \vec{u}_g = \frac{1}{\sqrt{2K_o^*}}(\vec{u}_o^* - \hat{Z} \times \vec{u}_o^*), \qquad (5)$$

where $K_o^* = Kf/|\vec{u}_o^*|^2$ is the dimensionless vertical eddy diffusivity, K is the dimensional vertical eddy diffusivity, $\vec{u}_o^*$ is a stress velocity defined by $\vec{\tau}_o = \rho_o|\vec{u}_o^*|\vec{u}_o^*$, and ρ_o is the ocean surface density. The dimensionless diffusivity K_o^* is taken to be constant, reflecting a linear dependence of the Ekman layer depth on the stress velocity. This is appropriate for IOBLs with no surface buoyancy forcing; non-zero surface buoyancy modifies the vertical profile of K in the IOBL (McPhee, 2008). Our model could be extended to accommodate an arbitrary K-profile if the surface buoyancy fluxes were known, but for simplicity in this study we assume zero surface buoyancy forcing.

We prescribe the air–ice, air–ocean, and ice–ocean stresses using quadratic drag relations,

$$\vec{\tau}_{ai} = \rho_a C_{ai}|\vec{u}_a|\vec{u}_a = \rho_a|\vec{u}_{ai}^*|\vec{u}_{ai}^*, \qquad (6a)$$

$$\vec{\tau}_{ao} = \rho_a C_{ao}|\vec{u}_a|\vec{u}_a = \rho_a|\vec{u}_{ao}^*|\vec{u}_{ao}^*, \qquad (6b)$$

$$\vec{\tau}_{io} = \rho_o C_{io}|\vec{u}_i - \vec{u}_o|(\vec{u}_i - \vec{u}_o) = \rho_o|\vec{u}_{io}^*|\vec{u}_{io}^*. \qquad (6c)$$

where ρ_a and ρ_o are the atmospheric and surface ocean density respectively. Here we have implicitly assumed that there exist thin turbulent boundary layers between the atmosphere and the ice floes, between the atmosphere and ocean leads, and between the bases of the ice floes and the top of the Ekman layer, all of which transfer momentum at a rate that varies quadratically with the vertical shear. We have further assumed that any momentum imparted to the ocean leads is transferred directly down to the Ekman layer below. More comprehensive treatments of the ice–ocean stress may be derived using Rossby similarity theory (McPhee 2008; 2012). However, this theory cannot be applied in the presence of leads between the sea ice floes, which continually change the surface boundary condition at any given point between a free surface and a rigid ice floe. In many previous studies, these stresses carry a turning angle to account for the effect of the Coriolis force in the boundary layer (Hibler 1979; Thorndike and Colony 1982; Bitz et al. 2002; Uotila et al. 2012). This is not necessary here because we use the ageostrophic 10-m winds, and we explicitly account for the ocean surface Ekman layer.

By combining the ice–ocean stress relation (6c), which can be rewritten as $\vec{u}_{io}^* = \sqrt{C_{io}}(\vec{u}_i -$

$\vec{u}_o$), with equation (5) for the shear across the Ekman layer, we obtain an expression for the total shear across the IOBL,

$$\vec{u}_i - \vec{u}_g = \frac{1}{\sqrt{C_{io}}}\vec{u}_{io}^* + \frac{1}{\sqrt{2K_0^*}}(\vec{u}_o^* - \hat{Z} \times \vec{u}_o^*). \tag{7}$$

Then, substituting (6a), (6c) and (7) into the momentum balance (3), we obtain a relationship between the unknown stress velocities $\vec{u}_{io}^*$ and $\vec{u}_o^*$,

$$\frac{\rho_i h_i f}{\sqrt{C_{io}}}\hat{Z} \times \vec{u}_{io}^* + \frac{\rho_i h_i f}{\sqrt{2K_0^*}}(\hat{Z} \times \vec{u}_o^* + \vec{u}_o^*) = \tag{8}$$
$$\varphi(\rho_a|\vec{u}_{ai}^*|\vec{u}_{ai}^* - \rho_o|\vec{u}_{io}^*|\vec{u}_{io}^*).$$

We require an additional equation to obtain an explicit solution for $\vec{u}_{io}^*$ and $\vec{u}_o^*$, so we rewrite the total stress at the base of the mixing layer (4) in the form

$$\rho_o|\vec{u}_o^*|\vec{u}_o^* = (1 - \varphi)\rho_a|\vec{u}_{ao}^*|\vec{u}_{ao}^* + \varphi\rho_o|\vec{u}_{io}^*|\vec{u}_{io}^*. \tag{9}$$

2.2 Model solution

We now solve equations (8) and (9), derived in the previous subsection, for the stress velocities $\vec{u}_{io}^*$ and $\vec{u}_o^*$, and thus for the ice velocity $\vec{u}_i$.

2.2.1   Near-100% sea ice cover ($\varphi \approx 1$)

We first consider the case of close to 100% sea ice cover ($\varphi \approx 1$) because this permits a closed-form analytical solution that offers physical intuition for the behavior of the model. Though an actual sea ice concentration of 100% would be inconsistent with our model, we will show in Sec. 4 that this provides a close approximation to the general solution for ice concentrations greater than 50%. The method of solution is very similar to that described by Leppäranta (2005), Ch. 6.1, but our explicit treatment of the oceanic boundary layer and prognostic determination of the turning angle warrant that the solution be given in full.

For sea ice concentrations close to 100% ($\varphi \approx 1$) equation (9) implies that the ice-ocean and ocean surface stress velocities are approximately equal, $\vec{u}_{io}^* \approx \vec{u}_o^*$. Thus equations (7) and (8) may be rewritten as

$$\vec{u}_i - \vec{u}_g = \left(\frac{1}{\sqrt{C_{io}}} + \frac{1}{\sqrt{2K_0^*}} \right) \vec{u}_{io}^* - \frac{1}{\sqrt{2K_0^*}} \hat{Z} \times \vec{u}_{io}^*, \tag{10a}$$

$$\left(\frac{\rho_i h_i f}{\sqrt{2K_0^*}} + \frac{\rho_i h_i f}{\sqrt{C_{io}}} \right) \hat{Z} \times \vec{u}_{io}^* + \frac{\rho_i h_i f}{\sqrt{2K_0^*}} \vec{u}_{io}^* = \rho_a |\vec{u}_{ai}^*| \vec{u}_{ai}^* - \rho_o |\vec{u}_{io}^*| \vec{u}_{io}^*. \tag{10b}$$

1 We simplify the coefficients by multiplying both sides of (10b) by $\sqrt{2K_0^*}/\rho_i h_i f$ and

2 rearranging to obtain

$$(\alpha + 1)\hat{Z} \times \vec{u}_{io}^* + (1 + k_o |\vec{u}_{io}^*|)\vec{u}_{io}^* = k_a |\vec{u}_{ai}^*| \vec{u}_{ai}^*, \tag{11}$$

3 where

$$\alpha = \sqrt{2K_0^*/C_{io}}, \ k_a = \rho_a \sqrt{2K_0^*}/\rho_i h_i f \ \text{and} \ k_o = \rho_o \sqrt{2K_0^*}/\rho_i h_i f. \tag{12}$$

4 To solve, we first define the components of $\vec{u}_{io}^*$ parallel and perpendicular to the wind stress

5 velocity, or, equivalently, perpendicular the 10 m winds:

$$u_{io}^{*\|} = \frac{\vec{u}_{ai}^*}{|\vec{u}_{ai}^*|} \cdot \vec{u}_{io}^*, \tag{13a}$$

$$u_{io}^{*\perp} = \left(\hat{Z} \times \frac{\vec{u}_{ai}^*}{|\vec{u}_{ai}^*|} \right) \cdot \vec{u}_{io}^*. \tag{13b}$$

6 Then taking the dot product of $\vec{u}_{io}^*$ with both sides of equation (11) and rearranging yields an

7 expression for $u_{io}^{*\|}$,

$$u_{io}^{*\|} = \frac{1}{k_a} \frac{|\vec{u}_{io}^*|^2}{|\vec{u}_{ai}^*|^2} (1 + k_o |\vec{u}_{io}^*|), \tag{14}$$

8 while taking the dot product of $\hat{Z} \times \vec{u}_{io}^*$ with both sides of (11) yields an expression for $u_{io}^{*\perp}$,

$$u_{io}^{*\perp} = -\frac{1}{k_a} \frac{|\vec{u}_{io}^*|^2}{|\vec{u}_{ai}^*|^2} (1 + \alpha). \tag{15}$$

9 Equations (14) and (15) do not constitute an explicit solution for $\vec{u}_{io}^*$ because they depend on

10 the magnitude $|\vec{u}_{io}^*|$. We determine this magnitude using the definition, $|\vec{u}_{io}^*|^2 = \left(u_{io}^{*\|}\right)^2 +$

11 $(u_{io}^{*\perp})^2$, which yields a quartic equation for $|\vec{u}_{io}^*|$,

$$k_o^2 |\vec{u}_{io}^*|^4 + 2k_o |\vec{u}_{io}^*|^3 + (1 + (\alpha + 1)^2)|\vec{u}_{io}^*|^2 = k_a^2 |\vec{u}_{ai}^*|^4. \tag{16}$$

12 In principle, this may be solved analytically for $|\vec{u}_{io}^*|$, but for the purposes of this study we

13 solve (11) numerically. Note that the right-hand side of (11) is a monotonically increasing

function of $|\vec{u}_{io}^*|$, so a unique solution exists for any wind stress velocity $|\vec{u}_{ai}^*|$. Having obtained the components of the stress velocity, it is straightforward to solve for the shear between the sea ice and the geostrophic ocean velocity using (10a).

2.2.2 Sparse sea ice cover ($\varphi \ll 1$)

We now consider sea ice concentrations much below 100%, for which it is would be inaccurate to assume $\varphi \approx 1$. In general there is no closed-form analytical solution to the model equations, and a solution must be obtained numerically. We begin by simplifying the coefficients in equations (8) and (9) by defining α, k_a, and k_o as in Sec. 2.1, and additionally defining $\beta = \rho_a C_{ao}/\rho_o C_{ai}$,

$$\alpha \hat{Z} \times \vec{u}_{io}^* + \hat{Z} \times \vec{u}_o^* + \vec{u}_o^* = \varphi k_a |\vec{u}_{ai}^*|\vec{u}_{ai}^* - \varphi k_o |\vec{u}_{io}^*|\vec{u}_{io}^*, \tag{17}$$

$$|\vec{u}_o^*|\vec{u}_o^* = (1 - \varphi)\beta|\vec{u}_{ai}^*|\vec{u}_{ai}^* + \varphi|\vec{u}_{io}^*|\vec{u}_{io}^*. \tag{18}$$

Here we have combined equations (6a) and (6b) to relate the atmosphere-ice and atmosphere-ocean stress velocities via $\vec{u}_{ai}^*/\sqrt{C_{ai}} = \vec{u}_{ao}^*/\sqrt{C_{ao}}$. Equations (17–18) may in principle be solved analytically following a procedure similar to that described in Sec. 2.2.1: by defining stress velocity components parallel and perpendicular to the atmospheric velocity, $u_{io}^{*\parallel}$, $u_{io}^{*\perp}$, $u_o^{*\parallel}$, and $u_o^{*\perp}$, analogously to definitions (13a) and (13b). Then taking the dot product of $\vec{u}_{ai}^*$ and $\hat{Z} \times \vec{u}_{ai}^*$ with each of (17) and (18) yields four scalar equations that can be solved simultaneously for the components of $\vec{u}_{io}^*$ and $\vec{u}_o^*$. Finally, using the definitions $|\vec{u}_{io}^*|^2 = \left(u_{io}^{*\parallel}\right)^2 + (u_{io}^{*\perp})^2$ and $|\vec{u}_o^*|^2 = \left(u_o^{*\parallel}\right)^2 + (u_o^{*\perp})^2$ yields a pair of equations that must be solved simultaneously for $|\vec{u}_{io}^*|$ and $|\vec{u}_o^*|$. In practice we simply solve (17–18) numerically using least-squares optimization.

2.3 Physical interpretation

Though equations (14–16) constitute an analytical solution to the mixture layer momentum balance (11), in this form they yield little insight into the wind-driven drift of sea ice. We therefore provide additional formulae for some key quantities describing the ice drift. Moreover, we briefly discuss the similarities and differences between our equations and the equations based on Rossby similarity theory (e.g. McPhee 2008; 2012). We base our discussion around the solution for near-100% sea ice concentration, given in section 2.2.1,

9

1   because this solution is completely analytical and thus offers more insight.

2.3.1 Ice velocity

3   For convenience we re-state equation (10a), which relates the shear between the ice and the
4   geostrophic ocean velocity to the ice-ocean stress velocity in the case of close to 100% sea
5   ice cover,

$$\vec{u}_i - \vec{u}_g = \left(\frac{1}{\sqrt{C_{io}}} + \frac{1}{\sqrt{2K_0^*}}\right)\vec{u}_{io}^* - \frac{1}{\sqrt{2K_0^*}}\hat{Z} \times \vec{u}_{io}^*.$$

6   This equation is similar to the one derived by McPhee (2008; 2012) for the case of an
7   unstratified IOBL, because both approaches assume a traditional Ekman layer solution over
8   most of the IOBL. However, there are some notable differences: Instead of assuming that the
9   turbulent transfer of momentum follows a quadratic drag law, McPhee (2008; 2012) utilized
10   the *law of the wall* equation across the ocean-ice boundary layer, leading to a slightly more
11   complicated version of this equation,

$$\vec{u}_i - \vec{u}_g = \left(\frac{1}{\kappa}\log\left(\frac{|\vec{u}_{io}^*|}{f z_0}\right) + \frac{1}{\kappa}\log\left(\frac{K_0^*}{\kappa}\right) + \frac{1}{\sqrt{2K_0^*}}\right)\vec{u}_{io}^* - \frac{1}{\sqrt{2K_0^*}}\hat{Z} \times \vec{u}_{io}^*,$$

12   where κ is Karman's constant ($\kappa = 0.4$) and z_0 is hydraulic roughness at the bottom of sea
13   ice. Because the velocity profile over the ocean-ice boundary layer is assumed to be
14   logarithmic (i.e. following the *law of the wall*), logarithmic terms appear as coefficients of
15   ice-ocean stress velocity $\vec{u}_{io}^*$. In our equation (10a) these terms are replaced by $1/\sqrt{C_{io}}$, due
16   to our assumption of a linear relationship between the ice-ocean shear and the ice-ocean
17   stress velocity.

18   Our formulation is arguably a less accurate description of the IOBL when the sea ice
19   concentration is close to 100% because it does not allow the ice speed to vary nonlinearly
20   with the ice-ocean stress velocity. However, in general the sea ice concentration may be
21   much smaller than 100%, and at any given horizontal location the surface boundary condition
22   is transient, varying between a solid upper boundary (the ice) and a free surface (open water).
23   Thus the assumption of a flow following the *law of the wall* and the notion of a hydraulic
24   roughness length no longer applies to this case. We have therefore assumed quadratic drag

laws at these interfaces for simplicity, but in principle a more accurate IOBL model could be derived following the ideas of Rossby similarity theory but using a transient surface boundary condition that varies between a solid boundary and a free surface.

2.3.2 Turning angles

The IOBL turning angle is the angle between the ice-ocean stress velocity $\vec{u}_{io}^*$ and the ice-geostrophic shear $(\vec{u}_i - \vec{u}_g)$, and may be defined as

$$\cos(\theta_{IOBL}) = \frac{\vec{u}_{io}^* \cdot (\vec{u}_i - \vec{u}_g)}{|\vec{u}_{io}^*||\vec{u}_i - \vec{u}_g|}. \tag{19}$$

In our model, the IOBL turning angle for near-100% sea ice concentration is

$$\cos(\theta_{IOBL}) = \frac{1 + \alpha}{\sqrt{1 + (1 + \alpha)^2}}, \tag{20}$$

which is independent of the surface wind speed and depends only on the parameter $\alpha = \sqrt{2K_0^*/C_{io}}$. Thus for near-100% sea ice concentration, prescribing an Ekman spiral and a linear relationship between the ice–ocean stress velocity $\vec{u}_{io}^*$ and the ice–ocean shear $(\vec{u}_i - \vec{u}_o)$ is equivalent to assuming a constant geostrophic ice-ocean turning angle (e.g. Hibler, 1979; Thorndike and Colony, 1982). By contrast the IOBL turning angle predicted by Rossby similarity theory varies as a function of the ice-ocean stress velocity, and the turning angle varies by a few degrees over a realistic range of ice–ocean stress magnitudes (McPhee, 1979; 2008).

Note that in our model θ_{IOBL} is generally not independent of the surface wind speed when the sea ice concentration is below 100%. Fig. 2 shows the IOBL turning angle θ_{IOBL} as a function of α. The IOBL turning angle θ_{IOBL} decreases from 45 degrees to zero as α increases from zero to infinity. A larger value of α corresponds to a relatively large vertical diffusivity K_0^*, which tends to reduce the magnitude of the shear in the Ekman layer. Thus the shear becomes dominated by the surface boundary layer, over which the shear does not turn with depth. A smaller value of α corresponds to a relatively large drag coefficient C_{io}, which tends to reduce magnitude of the shear in the surface boundary layer. Thus the shear becomes dominated by the Ekman spiral, over which the shear turns by 45 degrees. This is consistent with Rossby similarity theory (McPhee 2008; 2012) in that multi-year ice pack

11

1 with a relatively high basal hydraulic roughness corresponds to a larger a larger turning angle

2 θ_{IOBL}. In this study, we employ the canonical value of $K_o^* = 0.028$ (McPhee, 1994; 2008),

3 and we use C_{io}=0.0071 based on the estimate of Cole et al. (2014) from the ITP-V data. This

4 combination of K_o^* and C_{io} produces a θ_{IOBL} of around 15 degrees (red dot in Fig. 2). This

5 value is within the range of turning angles predicted by Rossby similarity theory, which is

6 about 20 degrees for multi-year ice pack and 13 degrees for the first-year ice (McPhee 2012).

7 We now turn to the ice drift itself. We derive the angle between the 10m wind speed $\vec{u}_a$ and

8 the ice-geostrophic shear $\vec{u}_i - \vec{u}_g$ by taking the dot product of $\vec{u}_{ai}^*$ with (10a), noting that

9 $\vec{u}_{ai}^*$ lies parallel to $\vec{u}_a$ from (6a), and using (14) and (15) for the components of $\vec{u}_{io}^*$,

$$\cos(\theta_{ai}) = \frac{k_o |\vec{u}_{io}^*|^2}{k_a |\vec{u}_{ai}^*|^2} \frac{1+\alpha}{\sqrt{1+(1+\alpha)^2}} = \frac{|\vec{\tau}_{io}|}{|\vec{\tau}_{ai}|} \cos(\theta_{IOBL}) \tag{21}$$

10 Using equation (16) above, it is straightforward to show that the ratio of the ice–ocean to air–

11 ice stresses is smaller than one, $k_o |\vec{u}_{io}^*|^2 / k_a |\vec{u}_{ai}^*|^2 = |\vec{\tau}_{io}|/|\vec{\tau}_{ai}| < 1$, so it follows that the

12 air–ice angle is always at least as large as the IOBL turning angle, $\theta_{ai} \geq \theta_{IOBL}$. This reflects

13 the fact that the 10-m wind velocity $\vec{u}_a$ always points to the left of the ice–ocean stress $\vec{\tau}_{io}$

14 (*c.f.* equations (14) and (15)), while the ice–geostrophic shear $\vec{u}_i - \vec{u}_g$ always points to the

15 right of $\vec{\tau}_{io}$ (*c.f.* equation (10a)). For strong winds ($|\vec{\tau}_{ai}| \to \infty$) equation (16) implies that the

16 air–ice and ice–ocean stresses balance one another in (3) (i.e. $\vec{\tau}_{io} \to \vec{\tau}_{ai}$), so the air-ice

17 turning angle becomes independent of the wind speed and equal to the IOBL turning angle.

18 For weak winds ($|\vec{\tau}_{ai}| \to 0$) equation (16) implies that the ice–ocean to air–ice stress ratio

19 vanishes[1], $|\vec{\tau}_{io}|/|\vec{\tau}_{ai}| \to 0$, so from (18) the ice velocity becomes directed 90° to the right of

20 the winds.

21

---

[1] To obtain this result from equation (16), first note that if $|\vec{u}_{ai}^*| = 0$ then the only non-negative real solution to (16) is $|\vec{u}_{io}^*| = 0$, so we can conclude that $|\vec{u}_{io}^*| \to 0$ as $|\vec{u}_{ai}^*| \to 0$. Then note that in the limit of vanishing air-ice stress, $|\vec{u}_{ai}^*| \to 0$, equation (16) can only remain balanced if $|\vec{u}_{io}^*| \sim |\vec{u}_{ai}^*|^2$. It follows that $|\vec{\tau}_{io}|/|\vec{\tau}_{ai}| \to 0$ as $|\vec{u}_{ai}^*| \to 0$.

3 Observation and Reanalysis Datasets

In this section we detail the various observational and reanalysis datasets used to evaluate our analytical model and to quantify how southerly winds affects Arctic summer sea ice concentration.

3.1 Observations

To evaluate our analytical model with observations, we used observations from an ice-tethered profiler (ITP; Toole et al., 2010) equipped with a velocity sensor (ITP-V; Williams et al., 2010). Specifically, we use data from ITP-V 35, which was deployed on October 8, 2009 on an ice floe in the Beaufort Sea at 77° N, 135° W, as part of the Beaufort Gyre Observing System (BGOS). The ice floe was 2.6 m thick, so hydrostatic adjustment resulted in an ice–ocean interface at around 2.3 m depth (Cole et al. 2014). Ocean velocity profiles were obtained every 4 h to 150 m depth, with an effective vertical resolution of 1 m. To examine the ice–ocean shear $(\vec{u}_i - \vec{u}_o)$ and the ice-ocean velocity angle, we use the shallowest measurements from the velocity profiles, at a depth of 7 m. The ice velocity $(\vec{u}_i)$ is derived from hourly GPS fixes and linearly interpolated in time to align with the time of the ITP-V 35 observations. Further details, including calibrations and a discussion of errors in ITP-V 35, are described by Cole et al. (2014).

Arctic sea ice concentration data is from the U.S. National Snow and Ice Data Center (NSIDC), and is based on satellite-derived passive microwave brightness temperature. Specifically, the NASA Team Algorithm (Swift and Cavalieri, 1985) was used to estimate the sea ice concentration. These data are provided as a daily mean on a polar stereographic grid with 25 x 25 km resolution. We re-gridded this data onto a regular 1.0° x 1.0° grid.

3.2 Reanalysis

Observations of Arctic sea ice thickness are sparse, so instead we use the coupled Pan-arctic Ice-Ocean Modeling and Assimilation System (PIOMAS; Zhang and Rothrock, 2003) to estimate the basin scale Arctic sea ice thickness. PIOMAS consists of a 12-category thickness and enthalpy distribution sea ice model coupled with the POP (Parallel Ocean Program) ocean model (Smith et al., 1992). The data is monthly and covers from the year 1978 to 2013. For the surface wind stress we used 10 m winds provided by the European Center for

Medium-Range Weather Forecasts ERA-Interim reanalysis dataset (Dee et al., 2011). The data is 6 hourly with a horizontal resolution of 1.0° x 1.0°.

4   Model evaluation

In this section, we evaluate our analytical model against the ITP-V 35 observations of sub-sea ice ocean velocity (Cole et al., 2014). Specifically, we compare the modeled wind-ice and ice-ocean velocity angles against the observed values. As outlined in the introduction, one might not expect the winter Beaufort Sea to serve as a useful test case because the sea ice concentration is typically close to 100%, so the internal stresses neglected in our model may be dynamically significant (Leppäranta, 2005). Additionally, sea ice formation in winter may produce negative buoyancy forcing that induces strong convection and vertically-varying eddy viscosity in the surface mixed layer, inconsistent with our assumption of as uniform vertical viscosity throughout the Ekman layer (McPhee, 2012). However, the ITP-V 35 measurements indicate that the ice was very close to a free drift regime and experienced weak vertical buoyancy fluxes in the surface mixed layer (Cole et al., 2014), so these features of the winter sea ice pack may be less prominent than in previous observations. For a complete picture of the stratification regime in the observed near-surface ocean, see figures 3, 4, 8 and 9 of Cole et al. (2014). For example, the mixed layer depth over the Beaufort Sea is very shallow in October (~15 m) and deepens to 30–40 m in February and March (Fig. 9 of Cole et al. 2014).

4.1   Model parameters

The ITP-V 35 was deployed upon a 2.6 m-thick ice floe, which is much thicker than the mean ice thickness over the western Beaufort Sea. Fig. 1a shows the PIOMAS sea ice thickness averaged from October 2009 to March 2010. During this time period, sea ice thickness over the western Beaufort Sea (around 74-78° N, 135-150° W) is around 1.4–1.6 m. It is therefore likely that ITP-V 35 was mounted on a relatively sturdy floe, whereas the surrounding floes were thinner. Sea ice concentration over this region is mostly over 85-90% from October to March (Fig. 1b). The velocity of the mixture layer (see Sec. 2) represents a bulk average over many floes, and similarly the ocean Ekman layer in any given location responds to stresses transmitted by a series of ice floes passing overhead. For the purpose of model evaluation we

therefore take the sea ice thickness h_i to be 1.5 m, which is appropriate for basin-scale sea ice momentum balance.

Extensive measurements of the ice-ocean boundary layer suggest that the annual mean value of the dimensionless vertical eddy diffusivity K_o^* is about 0.028 (McPhee, 1994; 2008). Below we also present model predictions using a nominal enhanced value of $K_o^* = 0.1$, which yields improved agreement between the model and the observations. A possible explanation for this is that the ITP-V observations mostly cover winter season (from October to March), when surface buoyancy loss due to sea ice formation can enhance the vertical eddy diffusivity by a factor of up to 10 (McPhee and Morison, 2001). However, it is more likely that internal stresses in the ice impede its motion, so the canonical value of $K_o^* = 0.028$ overestimates the ice drift. Thus the reader should not infer from our results that using a larger value of K_o^* is more physically realistic. Finally, the geostrophic current in the interior of polar oceans, $\vec{u}_g$, is poorly constrained, and we assume that this term is small relative to the surface current. This assumption should be more robust on intraseasonal time scales, as surface winds can strengthen rapidly in a few days, so the resultant surface Ekman velocity is likely to be much larger than the interior geostrophic flow.

For other parameters, we used standard values used in many previous studies: $\rho_a = 1.35 \text{ Kg}/m^3$, $\rho_i = 910 \text{ Kg}/m^3$, and $\rho_o = 1026 \text{ Kg}/m^3$. The atmospheric drag coefficients C_{ai} and C_{ao} depend on the season, the ice fraction, and the surface roughness (Lüpkes et al., 2012), but for simplicity we use a constant values of $C_{ai} = 1.89 \times 10^{-3}$ and $C_{ao} = 1.25 \times 10^{-3}$ (Lüpkes and Birnbaum, 2005). We prescribe the ice-ocean drag coefficient C_{io} based on the findings of Cole et al. (2014), who found that $C_{io} = 7.1 \times 10^{-3}$ best fit the ITP-V 35 measurements. However, we note that it is difficult to calculate C_{io} accurately from the ITP-V data because measurements of the vertical eddy momentum fluxes were made at a depth of 6 m, a few meters below the ice base.

4.2 Results

Fig. 3 shows the observed ice speed (black line) as a function of the 10 m wind speed. Consistent with Thorndike and Colony (1982), the relationship is linear, except for weak winds (speed less than 2 m/s). For moderately strong winds, sea ice moves with a speed

15

1   around 1.5–2% of the surface wind speed. This is consistent with or slightly weaker than the

2   well-known 2% relationship (Thorndike and Colony, 1982). Fig. 3a shows that the analytical

3   model with the canonical value of K_o^* ($K_o^* = 0.028$) overestimates the observed ice speed by

4   20–40%, whereas a larger vertical diffusivity (blue-dotted line; $K_o^* = 0.1$) fits better with the

5   observations. As stated above, this is probably because the internal stresses in the relatively

6   concentrated sea ice (85–100% in winter) impede the ice drift. We also compare the observed

7   ice drift speeds with those predicted by 'classical' fee drift (Leppäranta, 2005), in which we

8   neglect both the Ekman layer velocity and the geostrophic velocity. Mathematically this

9   corresponds to assuming an infinitely large vertical diffusivity ($K_o^* \to \infty$) in our model. This

10   classical free drift (blue solid line in Fig. 3a) is about 30% slower than the ice drift with an

11   interactive Ekman layer (red line in Fig. 3a), verifying that the IOBL substantially enhances

12   the wind-induced ice speed.

13   Fig. 3b shows that there is little difference in ice speed between 100% sea ice cover (red line;

14   $\varphi = 1$) and 50% sea ice cover (red line; $\varphi = 1$) in this model (Fig. 3b). As shown in

15   equation (10a), the ice-ocean drag coefficient, C_{io}, also directly influences the wind-induced

16   ice velocity. The bottom panels of Fig. 3 show the sensitivity of the ice speed to C_{io} for

17   $K_o^* = 0.1$ (Fig. 3c) and $K_o^* = 0.028$ (Fig. 3d) respectively. Decreasing C_{io} from 0.0071 to

18   0.004 increases ice speed up to 20–25%. In the Appendix we calculate C_{io} using the ITP-V

19   data and plotted C_{io} both as a function of 10 m wind speed and surface stress (Fig. A1).

20   Consistent with Cole et al. (2014), the individual observed values of C_{io} vary widely, by a

21   factor 10. In general, there is no obvious dependence of C_{io} on the surface stress, so we use

22   the constant value $C_{io} = 0.0071$ of Cole et al. (2014).

23   Fig. 4 shows that the wind–ice velocity angle θ_{ai} decreases as the surface wind strengthens,

24   consistent with previous observations (Thorndike and Colony, 1982). The velocity angle is

25   overestimated by 5–10 degrees in the case when the canonical vertical diffusivity $K_o^* =$

26   0.028 is used (Fig. 4a). The analytical model with $K_o^* = 0.1$ reproduces this curve

27   remarkably well. Recall from equation (21) that wind-ice velocity angle θ_{ai} decreases as the

28   ice-ocean to wind-ice stress ratio ($|\vec{\tau}_{io}|/|\vec{\tau}_{ai}|$) increases, and that this stress ratio is always

29   smaller than 1. Thus, the decrease of θ_{ai} with increasing surface wind speed indicates that

30   the stress ratio increases as the surface winds strengthen. In other words, the momentum

becomes more efficiently transferred down to the ocean as the surface wind speed increases. For relatively weak winds, the observational errors in θ_{ai} (gray shadings in Fig. 4) are large, whereas for stronger winds the air–ice velocity angle is much better constrained (Cole et al., 2014). The wind–ice velocity angle θ_{ai} estimated using the 'classical' free drift case is about 20 degrees smaller than that predicted by the canonical vertical diffusivity $K_o^* = 0.028$. Moreover, the classical free drift substantially underestimates the observed θ_{ai} even though the internal friction is neglected. This result indicates that the IOBL is essential for properly simulating the direction of the ice drift. Fig. 4b shows that sea ice cover plays a nontrivial role in changing the wind–ice velocity angle θ_{ai}, although the internal stress is neglected in the model. Decreasing sea ice cover from 100% ($\varphi = 1$) to 50% ($\varphi = 0.5$) increases θ_{ai} by 20 degrees for large wind speeds.

The shallowest measurement depth of ITP-V 35 is 7 m, which is far below the ice base (~2.6 m). The Ekman spiral rotates the velocity substantially between the ice base and 7 m. Consequently the ITPV data is not suitable for estimating the IOBL turning angle. Instead we test our analytical treatment of the IOBL using the velocity angle between the ice floe and the ocean at 7 m, $\theta_{io}|_{z=-7\text{m}}$. To calculate $\theta_{io}|_{z=-7\text{m}}$ from the analytical model, the velocity angle needs to be adjusted using the Ekman layer solution, which can be written as a function depth, z, as

$$\vec{u}(z) = \vec{u}_o \exp\left(\frac{z + h_o}{\delta_E}\right) \exp\left(i\frac{z + h_o}{\delta_E}\right) \tag{22}$$

Here $\vec{u}_o$ is the ocean surface velocity at the bottom of sea ice, $h_o = (\rho_i/\rho_o)h_i$ is the depth of the ice base, and $\delta_E = \sqrt{2K/f}$ is the Ekman depth. We have used complex variables to describe two-dimensional vectors, $e.g.$ $\vec{u}_o = (u_o, v_o) \equiv u_o + iv_o$, because this presents changes in vector orientation more intuitively. The complex term, $\exp(i(z + h_o)/\delta_E)$, produces a velocity $\vec{u}|_{z=-d}$ at any depth d that is rotated relative to $\vec{u}_o$ by a clockwise angle of $(d - h_o)/\delta_E$ radians. Thus the adjusted velocity angle between the ice and the ocean at any depth in the Ekman layer is:

$$\theta_{io}|_{z=-d} = \theta_{io}|_{z=-h_o} + (d - h_o)/\delta_E \tag{23}$$

In Fig. 5 we plot $\theta_{io}|_{z=-7\text{m}}$ as a function of the ice speed, comparing the predictions of our model with the data from Cole et al. (2014). In general, the ice–ocean velocity angle

17

1   $\theta_{io}|_{z=-7\text{m}}$ decreases as ice speed increases. Consistent with Cole et al. (2014), the variance

2   in the observationally derived values of $\theta_{io}|_{z=-7\text{m}}$ is quite large, especially for low ice

3   speeds. Our analytical solution for the ice-ocean velocity angle, adjusted using equation (23),

4   agrees reasonably well with the ITP-V 35 measurements. Again, the analytical model predicts

5   the observational curve better when the higher vertical diffusivity of $K_o^* = 0.1$ is used. Fig.

6   5b shows that ice concentration is certainly a factor affecting the ice-ocean velocity angle,

7   θ_{io}. Decreasing sea ice cover from 100% to 50% causes a decrease in θ_{io} because the

8   direction of ice drift is constrained by the wind stress over open water between the ice floes

9   $(\vec{\tau}_{ao})$ and the associated surface Ekman transport.

10   ## 4.3 Parameter sensitivity

11   Having evaluated our model against the ITP-V 35 measurements using the best available

12   estimates for the model parameters, we now explore the sensitivity of the model's predictions

13   to key physical properties of the sea ice itself, namely its thickness and concentration. In Fig.

14   6 we plot the sensitivity of the wind-ice velocity angle (θ_{ai}) and the IOBL turning angle

15   (θ_{IOBL}) to a range of sea ice concentrations (φ) and ice thicknesses (h_i). In general, the wind-

16   ice velocity angle increases substantially with sea ice thickness (Fig. 6a): for a moderate wind

17   speed of 6 m/s, increasing the sea ice thickness from 0.25 m to 3 m increases this angle from

18   20° to 60°. It can therefore be inferred from equation (21) and Fig. 6a that thicker ice has

19   smaller stress ratio $|\vec{\tau}_{io}|/|\vec{\tau}_{ai}|$, implying that thicker ice is less efficient in transferring the

20   momentum into the ocean, leading to larger wind-ice velocity angle. In other words, thicker

21   ice absorbs more of the wind-input momentum into the Coriolis torque, transmitting less to

22   the ocean below.

23   Sea ice concentration also strongly influences these angles. Consistent with Fig. 4b, Fig. 6b

24   shows that wind-ice velocity angle increases as sea ice concentration decreases. There is little

25   difference in this angle between 100% and 75% ice concentrations – the angle is less

26   sensitive to relatively high sea ice concentration. However, the angle rapidly increases as sea

27   ice concentration gets below 50%: at 25% sea ice concentration the wind-ice angle is 20°

28   larger than at 100% concentration, even for the strongest winds in the dataset. The response

29   of the IOBL turning angle to the mixture of sea ice and water $(\varphi \ll 1)$ is rather surprising

18

(Fig. 6d). The turning angle is negative for weaker surface winds in the case when sea ice concentration is less than 100%. This is because wind stress over the ice-free component of the mixture layer is transmitted directly to the water below. As the sea ice concentration approaches zero, the stress transmitted through the ice becomes negligible in determining the direction of the surface Ekman velocity ($\vec{u}_o$). Because the ITP-V 35 track covers mostly ice-covered regions ($\varphi \approx 1$) and the shallowest measurement depth is 7 m, it is difficult to verify whether negative IOBL turning angles appear in the observations.

5   Application to wind-driven summer sea ice changes

In this section, we quantify the effect of intra-seasonal southerly wind strengthening events on Arctic sea ice cover using near-surface wind data, and compare the results with satellite observations. There are several notable Arctic weather perturbations in the spring and summer over the Pacific sector of the Arctic Ocean, such as the development of the Arctic dipole mode (Wu et al., 2006), quasi-stationary cyclonic winds (Serreze et al., 2003) and synoptic cyclones (Zhang et al., 2013). These perturbations are often accompanied by rapid strengthening of southerlies and a reduction of the sea ice concentration (SIC) on intraseasonal time scales. In the Arctic summer, sea ice thickness is mostly below 2 m (Fig. 7a) and the area of the marginal ice zone with a moderate SIC (25–75%) is quite large (Fig. 7b). We therefore hypothesize that the strengthening of southerlies should efficiently redistribute the sea ice cover in the summer.

This analysis simultaneously serves as an additional evaluation of our analytical model described in Sec. 2. Our model is particularly appropriate to motions in the marginal ice zone, where internal stress is negligible, and to short-duration intensification of the southerly winds, during which the surface ocean velocity will typically be large compared to the geostrophic velocity. This evaluation could in principle be extended to compare the modeled sea ice velocities directly against sea ice drift products. However, we have chosen to retain our focus on the sea ice concentration rather than the ice drift velocity. Ice drift products exhibit considerable uncertainty, particularly during summer when the ice is typically thinner (Sumata et al., 2014). Furthermore, there is considerable variance in the ice speed and the

1   wind-ice velocity angle even in the ITP-V data (see Figs. 3 and 4), in which the ice velocities

2   are measured accurately using GPS fixes.

3   ## 5.1 Methods

4   For surface wind forcing, we used the ERA-Interim reanalysis. Arctic sea ice concentration

5   data is from the U.S. National Snow and Ice Data Center (NSIDC). The Arctic sea ice

6   concentration shows multi-decadal declining trend and this trend was removed for each

7   calendar day and for each grid. For sea ice thickness, we used the climatological mean

8   PIOMAS sea ice thickness data averaged from 1990 to 2012.

9   Using the analytical solutions derived in Sec. 2, sea ice velocity is calculated from the ERA-

10 Interim daily 10 m winds. Then, lagged composite analyses are performed in order to

11 investigate how a rapid development of southerlies affects sea ice concentration during the

12 Arctic summer. We used data from 1990 to 2012 and focused on the summer, from August 1

13 to September 30 (AS). To define the events of the rapid strengthening of southerlies, the

14 surface winds over the Pacific sector of the Arctic are zonally and meridionally averaged,

15 from 150°E to 230°E and from 70°N to 90°N (cosine weighting is applied to each latitude).

16 Then, the southerly wind event is defined as a time period when the averaged southerly wind

17 value exceeds 1 standard deviation for three or more consecutive days. If the beginning of an

18 event occurs within 7 days of the end of the preceding event, then the latter event is discarded.

19 This procedure identifies 27 events during the analysis period. Lag zero is defined as the day

20 when the averaged southerly winds peak. Prior to generating the composites, a 3-day moving

21 average is applied to filter out noise associated with day-to-day fluctuations.

22 These southerly wind-induced sea ice drifts redistribute sea ice concentration. This effect is

23 computed using the following evolution equation: $dI_c = -\left[\frac{\partial(U_i I_c)}{\partial x} + \frac{\partial(V_i I_c)}{\partial y}\right] dt$. Here I_c is

24 sea ice concentration, which ranges from 0 to 1, at each grid point, and dt is a time step,

25 which has a length of one day in this study. To calculate sea ice concentration anomalies we

26 subtract the long-term climatological mean dI_c from the daily dI_c during the southerly

27 wind events. Then, the anomalous daily dI_c is integrated from the lag day -8 to estimate the

28 cumulative changes in sea ice concentration associated with the southerly wind events:

$$\Delta I_c = -\sum_{t=-8}^{t=lag} (dI_c)' d\mathrm{t} - \sum_{t=-8}^{t=lag} \left[\frac{\partial(U_i I_c)}{\partial x} + \frac{\partial(V_i I_c)}{\partial y} \right]' d\mathrm{t} \qquad (24)$$

1   Here, prime $(\ )'$ denotes a deviation from the long-term climatological mean. The time

2   integration starts from the lag -8 because the southerly wind events, on average, start about a

3   week before they peak. The results we present are not very sensitive to the starting date. The

4   maximum and the minimum values of the cumulative changes in sea ice concentration (ΔI_c)

5   are limited by the mean sea ice concentration, which ranges between 0% and 100%. For

6   example, if the cumulative changes in the mean sea ice concentration ($\Delta I_c + \overline{I_c}$), where $\overline{I_c}$ is

7   the climatological-mean sea ice concentration, exceeds 100%, then ΔI_c is given as

8    $(100 - \overline{I_c})$ %. All of the analytical model results presented here use the canonical value of

9   vertical diffusivity ($K_o^* = 0.028$) and the ice-ocean drag coefficient of $C_{io} = 0.0071$ (Cole

10   et al. 2014). As shown in Fig. 3, the wind-induced ice speed is sensitive to both K_o^* and C_{io}.

11 **5.2 Results**

12   Fig. 8 illustrates the response of the SIC (shadings in the left column) to the development of

13   southerlies (vectors in the left column) from the East Siberian and Chukchi Sea. Over a 10

14   day period since the development of southerlies, the SIC in these regions decreases by 7–8%.

15   The relative timing suggests that the reduction of SIC is caused by the southerly wind-

16   induced sea ice drift. In the meantime, because of cross-polar flow, SIC on the Atlantic sector

17   slightly increases (blue color). To further test this possibility, the wind-induced redistribution

18   of SIC is calculated using our model, specifically equations (17–18). The result, shown in the

19   right column of Fig. 8, captures the spatial pattern in the observed SIC anomalies. The

20   anomalous sea ice velocity (vectors in the right column) is generally directed towards the

21   Beaufort Sea, a little east of the surface wind velocity with the drift angle ranging between

22   20° and 45°. The calculated SIC anomalies at day +6 (bottom row of Fig. 8) are largely

23   consistent with the satellite observed SIC anomalies. However, the calculated SIC anomalies

24   somewhat underestimate the observation. At day +6, the calculated reduction of SIC over the

25   Pacific sector is about 5–6%, whereas the observed reduction of SIC is up to 6–8%. The

26   increase in SIC over the Atlantic sector associated with cross-polar flow is also slightly

27   underestimated.

1

2 There are several possible explanations for the discrepancy between the modeled and

3 observed sea ice concentration anomalies. Over the Atlantic sector, the cross-polar flow

4 increases SIC and the internal stress is likely to increase as well. As mentioned earlier, our

5 analytical model neglect internal stress that can decelerate ice drift and pile up sea ice over

6 the Atlantic sector. It is possible that the real sea ice thickness in the Arctic summer is thinner

7 than the PIOMAS sea ice thickness. While PIOMAS simulates the Arctic sea ice thickness

8 within a reasonable range, the model is known to generally *overestimate the thickness* of

9 measured sea ice thinner than 2 m (Johnson et al. 2012; Schweiger et al. 2011). Or, the

10 vertical diffusivity K_o^* in August and September might be smaller than 0.028 due to surface

11 buoyancy input resulting from sea ice melt (McPhee and Morison, 2001). The formation of a

12 summer freshwater layer at the ice base can also reduce the ice-ocean drag coefficient C_{io}

13 (Randelhoff et al., 2014), as can changes shape of the ice base. Additionally, the atmosphere-

14 ice drag coefficient may be larger during the summer season due to additional form stress

15 associated with the formation of leads and melt ponds (Lüpkes et al., 2012).

16

17 Finally, we ask: to what extent does the IOBL accelerate the wind-induced ice drift? We have

18 neglected the ocean surface geostrophic velocity in our analytical model calculations,

19 retaining only the surface Ekman layer. However, if the Ekman layer velocity were

20 sufficiently weak compared to the ice velocity then we could simply neglect the ocean

21 velocity altogether. As introduced in Sec. 4, the 'classical' fee drift (zero Ekman layer

22 velocity) corresponds mathematically to the limit of infinitely large vertical diffusivity

23 ($K_o^* \to \infty$) in our model. In Fig. 9 we compare the anomalous sea ice speed associated with

24 the wind-induced ice drift with and without an IOBL included in the model. Both curves have

25 been generated by averaging the sea ice speed anomalies over the Pacific sector of the Arctic

26 (from 150°E to 230°E and from 70°N to 90°N), and then calculating lagged composites

27 across all southerly wind events. Consistent with Fig. 3a, this plot illustrates that the IOBL

28 enhances the wind-induced sea ice speed up to 40-50%. We therefore conclude that the IOBL

29 plays a substantial role in the rapid reduction of SIC associated with strong southerly wind

30 events.

31

6   Summary and discussion

In this study we have derived an analytical model for wind-induced sea ice drift and evaluated our model against measurements from a velocity sensor-equipped ice-tethered profiler (ITP-V). We then used the model to demonstrate that Arctic southerly wind events can drive substantial reductions in sea ice concentration over short timescales.

Our model has elements in common with Rossby similarity theory (McPhee, 2008) for the ice–ocean boundary layer (IOBL), but differs crucially in the respect that it allows for an arbitrary mixture of ice and open water. The key features of this model are:

1. The ice floes and leads containing open water are described via a bulk "mixture layer", momentum balance, following Gray and Morland (1994).

2. The IOBL consists of an Ekman layer whose depth is assumed to depend linearly on the surface stress velocity (McPhee, 2011), most appropriate for a neutrally stratified IOBL with no surface buoyancy flux (McPhee and Morison, 2001).

3. The transfer of momentum between the 10 m winds, the ice and ocean components of the mixture layer, and the ocean surface layer are assumed to follow a quadratic drag laws. By contrast Rossby similarity theory assumes the 'law of wall' to hold in a narrow boundary layer at the top of the IOBL (McPhee, 2008).

Though the simplicity of our model carries several caveats, discussed below, it also confers several advantages. As mentioned in the introduction, the analytical tractability of the model makes it very efficient, certainly much more so than running a fully coupled model of the Arctic. This makes the model straightforward to interpret; the analytical expressions in Sec. 2 yield physical insight into the velocity observations from ITP-V 35 and the sea ice concentration data from NSIDC. The model's "mixture layer" formulation (Gray and Morland, 1994) also makes it suitable for the marginal ice zone. Our analytical approach was possible because we assumed a constant vertical diffusivity in the surface Ekman layer. This simplification results in an IOBL turning angle (θ_{IOBL}) that is independent of ice–ocean stress $\vec{u}_{io}^*$ in our model, whereas the turning angle slightly decreases as the ice–ocean stress strengthens in observations (McPhee 2008). It may be possible to extend our model to incorporate Rossby similarity theory and a stratified IOBL, but for sea ice concentrations below 100% the surface boundary condition must be modified to account for the presence of

patches of open water between the ice floes. Importantly, we also neglected internal stresses in the ice, which can feature prominently in the momentum balance when the sea ice concentration is close to 100% (Leppäranta, 2005).

Our analytical model qualitatively reproduces the wind-induced ice speed and wind-ice velocity angles in the ITP-V 35 observations. The agreement is improved by replacing the canonical value $K_o^* = 0.028$ of the vertical eddy diffusivity with an enhanced value of $K_o^* = 0.1$. However, this finding should not be interpreted to mean that the enhanced diffusivity is more physically relevant; while the discrepancy between the model and observations may be due to stronger turbulent mixing due to surface buoyancy loss, it is more likely due to impedance of the sea ice motion by internal stress.

We applied our analytical model to investigate the strong southerly events in the Arctic summer to estimate the wind-induced reduction of SIC. The calculated reduction of SIC is largely consistent with satellite observations. Our results verify that the southerly wind-induced sea ice drift can substantially decrease SIC over the course of a week. Because the wind-induced sea ice drift can be directly calculated from our analytical solution, the underlying processes for the sea ice variability might be better identified by utilizing reanalysis data. We suggest that our analytical model can be a flexible tool for identifying and quantifying the mechanisms for the Arctic and Antarctic sea ice cover variability, which is often associated with the changes in the global-scale circulation pattern (Lee et al. 2011; Holland and Kwok 2012; Bitz and Polvani 2012; Li et al. 2014; Wettstein and Deser 2014; Raphael and Hobbs 2014; Park et al. 2015).

Cole for assistance with the ITP-V 35 observational dataset.

Appendix

In this appendix we calculate the ice-ocean drag coefficient, C_{io}, using the ITP-V data. The ITP-V was programed to record turbulent fluctuations at 6 m depth for 40 minutes on a daily basis. As noted by Cole et al. (2014), C_{io} can be estimated by the relationship between ice-ocean velocity shear and turbulent momentum flux:

$$\sqrt{\overline{u'w'^2} + \overline{v'w'^2}} = \rho_o C_{io}[(u_i - u_6)^2 + (v_i - v_6)^2].$$ (A1)

Here the overbar $\overline{(\ )}$ denotes a 40-minute time average and the primes $(\ )'$ denote deviations from the time mean. The ice and 6 m ocean velocities are denoted as $(u_i,\ v_i)$ and $(u_6,\ v_6)$ respectively. Using equation (A1), we calculated daily C_{io} from the ITP-V data, following Cole et al. (2014). In Fig. A1 we plot C_{io} as a function of the surface wind speed and the surface stress.

References

Bitz, C. M., Fyfe, J., and Flato, G.: Sea ice response to wind forcing from AMIP models, *J. Climate*, **15**, 522–536, 2002.

Bitz, C.M. and Polvani, L. M.: Antarctic Climate Response to Stratospheric Ozone Depletion in a Fine Resolution Ocean Climate Model. *Geophys. Res. Lett.*, **39**, L20705, 2012.

Cole, S. T., Timmermans, M-L., Toole, J. M., Krishfield, R. A., and Thwaites, F. T.: Ekman Veering, Internal Waves, and Turbulence Observed under Arctic Sea Ice, *J. Phys. Oceanogr.*, **44**, 1306–1328, 2014.

Dee, D. P. *et al.*: The ERA-Interim reanalysis: Configuration and performance of the data assimilation system. *Quart. J. Roy. Meteorol. Soc.* **137**, 553–597, 2011.

Gray, J. M. N. T. and Morland, L. W.: A two-dimensional model for the dynamics of sea ice. *Phil. Trans. R. Soc. Lond. A*, **347**, 219–290, 1994.

Hibler, W. D. III.: A dynamic thermodynamic sea ice model. *J. Phys. Oceanogr.*, **9**, 815–846, 1979.

Heorton, D. B. S., Feltham, D. L., and Hunt, J. C. R.: The Response of the Sea Ice Edge to Atmospheric and Oceanic Jet Formation, *J. Phys. Oceanogr.*, **44**, 2292–2316, 2014.

Holland, P. R. and Kwok, R.: Wind-driven trends in Antarctic sea ice drift, *Nature Geosci.* **5,** 872–875, 2012.

Johnson, M., Proshutinsky, A. et al.: Evaluation of Arctic sea ice thickness simulated by Arctic Ocean Model Intercomparison Project models, *J. Geophys. Res*., **117**, C00D13, doi:10.1029/2011JC007257, 2012.

Kawakuchi, Y. and Mitsudera, H.: A numerical study of ice-drift divergence by cyclonic wind with a Lagrangian ice model. *Tellus*, **60A**, 789–802, 2008.

Lee, S., Gong, T. T., Johnson, N. C., Feldstein, S. B., and Pollard, D.: On the possible link between tropical convection and the Northern Hemisphere Arctic surface air temperature change between 1958-2001. *J. Clim*. **24**, 4350–4367, 2011.

Leppäranta, M.: The Drift of Sea Ice, Springer-Verlag, Berlin, 2005.

Li, X., Holland, D. M., Gerber, E. P., and Yoo, C.: Impacts of the north and tropical Atlantic Ocean on the Antarctic Peninsula and sea ice. *Nature*, **505**, 538–542, 2014.

Liptak, J. and Strong, C.: The winter atmospheric response to sea ice anomalies in the Barents Sea, *J. Clim*., **27**, 914–924, 2014.

Lüpkes, C. and Birnbaum, G.: Surface drag in the Arctic marginal sea ice zone: a comparison of different parameterisation concepts. *Boundary-Layer. Meteor.*, **117**, 179–211, 2005.

Lüpkes, C., Gryanik, V. M., Hartmann, J., and Andreas, E. L.: A parametrization, based on sea ice morphology, of the neutral atmospheric drag coefficients for weather prediction and climate models, *J Geophys. Res.*, **117,** D13, 2012.

McPhee, M. G.: The effect of the oceanic boundary layer on the mean drift of pack ice: Application of a simple model. *J. Phys. Oceanogr*., **9**, 388–400, 1979.

McPhee, M. G.: An analytic similarity theory for the planetary boundary layer stabilized by surface buoyancy. *Boundary-Layer Meterol*., **21**, 325−339, 1981.

McPhee, M. G.: On the turbulent mixing length in the oceanic boundary layer. *J. Phys. Oceanogr*. **24**, 2014−2031, 1994.

McPhee, M. G. and Morison, J. H.: Under-ice boundary layer. *Encyclopedia of Ocean Sciences*, 3069−3076, Elsevier, 2001.

McPhee, M. G.: *Air-ice-ocean interaction: turbulent ocean boundary layer exchange processes*, Springer, chapters 4 and 9, 2008.

McPhee, M. G.: Advances in understanding ice–ocean stress during and since AIDJEX, *Cold Reg. Sci. Technol.*, **76**, 24−36, 2012.

Ogi, M. and Wallace, J. M.: The role of summer surface wind anomalies in the summer Arctic sea ice extent in 2010 and 2011, *Geophys. Res. Lett*., **39**, L09704, 2012.

Park, H.-S., Lee, S., Son, S.-W., Feldstein, S. B. and Kosaka, Y.: The impact of poleward moisture and sensible heat flux on Arctic winter sea ice variability, *Journal of Climate*, **28,** 5030-5040, 2015.

Pedlosky, J.: *Geophysical Fluid Dynamics* (second edition), Springer-Verlag, pp. 227−232, 1987.

Plueddemann, A. J., Krishfield, R., Takizawa, T., Hatakeyama, K., and Honjo, S.: Upper ocean velocities in the Beaufort Gyre. *Geophys. Res. Lett.,* **25**, 183–186, 1998.

Raphael, M. N. and Hobbs, W.: The influence of the large-scale atmospheric circulation on Antarctic sea ice during ice advance and retreat seasons, *Geophys. Res. Lett*., 10.1002/2014GL060365, 2014.

Randelhoff, A. and Sundfjord, A. and Renner, A. H. H.: Effects of a Shallow Pycnocline and Surface Meltwater on Sea Ice--Ocean Drag and Turbulent Heat Flux. *Journal of Physical Oceanogr.*, **44**, 2176-2190, 2014.

Schweiger, A., Lindsay, R., Zhang J., Steele M., Stern, H., and Kwok, R.: Uncertainty in modeled Arctic sea ice volume, *J. Geophys. Res.*, **116**, C00D06, doi:10.1029/2011JC007084, 2011.

Serreze, M. C., Maslanik, J. A., Scambos, T. A., Fetterer, F., Stroeve, J., and co-authors.: A record minimum arctic sea ice extent and area in 2002. *Geophys. Res. Lett.*, **30**, 1110, 2003.

Smith, R. D., Dukowicz, J. K., and Malone, R. C.: Parallel ocean general circulation modeling, *Phys. D.*, **60**, 38–61, 1992.

Sorteberg, A. and Kvingedal, B.: Atmospheric forcing on the Barents Sea winter ice extent, *J. Clim.*, **19**, 4772–4784, 2006.

Sumata, H., T. Lavergne, F. Girard-Ardhuin, N. Kimura, M. A. Tschudi, F. Kauker, M. Karcher, and R. Gerdes.: An intercomparison of Arctic ice drift products to deduce uncertainty estimates, *J. Geophys. Res. Oceans*, **119**, 4887–4921, (2014).

Swift, C. T. and Cavalieri, D. J.: Passive microwave remote sensing for sea ice research. *Trans. AGU* **66**, 1210–1212, 1985.

Thorndike, A. S. and Colony, R.: Sea ice motion in response to geostrophic winds. *J. Geophys. Res.* **87**, 5845–5852, 1982.

Toole, J. M., Timmermans, M.-L., Perovich, D. K., Krishfield, R. A., Proshutinsky, A., and Richter-Menge, J. A.: Influences of the ocean surface mixed layer and thermohaline stratification on Arctic sea ice in the central Canada Basin. *J. Geophys. Res.*, **115**, C10018, doi:10.1029/2009JC005660, 2010.

Uotila, P., O'Farrell, S., Marsland, S. J., and Bi, D.: A sea ice sensitivity study with a global ocean-ice model. *Ocean Modelling*, **51**, 1–18, 2012.

Wettstein J. J. and Deser, C.: Internal Variability in Projections of Twenty-First-Century Arctic Sea Ice Loss: Role of the Large-Scale Atmospheric Circulation. *J. Clim*, **27**, 527−550, 2014.

Williams, A. J., Thwaites, F. T., Morrison, A. T., Toole, J. M., and Krishfield, R.: Motion tracking in an acoustic point-measurement current meter. *Proc. OCEANS 2010 IEEE*, Sydney, Australia, IEEE, 1−8, doi:10.1109/OCEANSSYD.2010.5603862., 2010.

Wu, B., Wang, J., and Walsh, J. E.: Dipole anomaly in the winter Arctic atmosphere and its association with sea ice motion, *J. Clim*, **19**, 210–225, 2006.

Zhang, J., and Rothrock, D. A.: Modeling global sea ice with a thickness and enthalpy distribution model in generalized curvilinear coordinates, *Mon. Weather Rev*., **131**, 681–697, 2003.

1   **Figure Captions**

2   **Figure 1**: **(a)** sea ice thickness (m) and **(b)** sea ice concentration (%), averaged from October

3   2009 to March 2010. Sea ice thickness is from PIOMAS and sea ice concentration data is

4   from NSDIC.

5

6   **Figure 2**: Sensitivity of the IOBL turning angle (θ_{IOBL}) to α $(= \sqrt{2K_0^*/C_{io}})$, calculated from

7   equation (20). The red dot corresponds to the canonical value for the vertical eddy diffusivity

8   (K_o^* =0.028) and blue dot corresponds to a nominal enhanced value (K_o^* = 0.1).

9

10   **Figure 3**: Sensitivity of ice speed (cm/s) to 10 m wind speed (m/s). The black line shows the

11   mean value calculated from ITP-V 35 observations binned by 10 m wind speed, and the gray

12   shadings indicate the range of one standard deviation from the mean. The red, dotted blue and

13   solid blue lines correspond to our analytical model, described in Sec. 2, with **(a)** vertical

14   diffusivities K_o^* = 0.028, 0.1 and ∞ (no IOBL) respectively. The sensitivity of the ice speed

15   to the ice concentration (φ) is shown in **(b)**; the red and blue lines indicate 100 % ice cover

16   ($\varphi = 1$) and 50% ice cover ($\varphi = 0.5$) respectively. The bottom panel shows the sensitivity of

17   ice speed to ice-ocean drag coefficient (C_{io}), with vertical diffusivities **(c)** K_o^* = 0.028 and **(d)**

18   K_o^* = 0.1 respectively. The bulk sea ice thickness is taken to be 1.5 m.

19

20   **Figure 4**: The velocity angle (clock-wise rotation angle) between the 10 m winds and the

21   ITPV-35 ice floe as functions of the 10 m wind speed (m/s). Note that typically the ice

22   velocity lies to the right of the wind velocity. In each plot the black line is mean observed

23   value from the ITP-V 35 dataset, binned by wind speed and ice speed respectively, and the

24   gray shadings indicate the range of one standard deviation from the mean. In **(a)**, the red,

25   dotted blue and solid blue lines correspond to our analytical model, described in Sec. 2, with

26   vertical diffusivities K_o^* = 0.028, 0.1 and ∞ (no IOBL) respectively. In **(b)**, the red and blue

27   lines correspond to 100% ($\varphi = 1$) and 50% ($\varphi = 0.5$) sea ice concentrations, in each case

28   using the canonical vertical diffusivity K_o^* = 0.028.

29

30   **Figure 5**: The velocity angle (clock-wise rotation angle) between the ice floe and the ocean

31   velocity at 7 m depth, as functions of the ice speed (cm/s). In each plot the black line is mean

observed value from the ITP-V 35 dataset, binned by wind speed and ice speed respectively, and the gray shadings indicate the range of one standard deviation from the mean. In **(a)**, the red and blue lines correspond to our analytical model, described in Sec. 2, with vertical diffusivities $K_o^* = 0.028$ and 0.1 respectively, and using 100 % ice concentration, $\varphi = 1$. In **(b)**, the red and blue lines correspond to 100% ($\varphi = 1$) and 50% ($\varphi = 0.5$) sea ice concentrations, in each case using the canonical vertical diffusivity $K_o^* = 0.028$.

Figure 6: Sensitivity of **(a, b)** wind-ice velocity angle and **(c, d)** IOBL turning angle to various values of **(a, c)** sea ice thickness h_i (m) and **(b, d)** sea ice concentration (φ) as a function of 10 m wind speed (abscissa; m/s). In all panels the dimensionless vertical diffusivity is fixed at $K_o^* = 0.028$. In **(a, c)** we use 100% sea ice concentration ($\varphi = 1$), and in **(b, d)** we use a sea ice thickness of $h_i = 1.5$ m.

Figure 7: Aug-Sep climatological mean **(a)** sea ice thickness (m) and **(b)** sea ice concentration (%) between 1990 and 2012. Sea ice thickness is from PIOMAS and sea ice concentration data is from NSDIC.

Figure 8: Composites of the anomalous sea ice concentration (%) calculated from NSIDC satellite observations (left column) and from our analytical model using ERA-Interim 10 m wind velocity data (right column) for lag -2 days (first row), 0 days (second row), 2 day (third row), and lag +6 days (fourth row). See Sec. 5 for a full description of this calculation. Vectors indicate the anomalous 10m winds from reanalysis (m/s; left column) and calculated sea ice velocity (cm/s; right column). For the anomalous 10m winds (left column) and sea ice velocity (right column), only vectors stronger than 1.5 m/s and 3.0 cm/s are plotted respectively.

Figure 9: Lagged composite of the calculated sea ice speed (cm/s) associated with the strong southerly events in the presence (red line) and in the absence (black line) of an IOBL in our analytical model (in the absence of an Ekman layer the ocean surface velocity is simply set to zero – the classical free drift case). The sea ice speed is area-averaged over the Pacific sector of the Arctic (from 150°E to 230°E and from 70°N to 90°N). The sea ice speeds that include

1   the surface Ekman layer (red line) identical to those used to construct Fig. 8. The

2   dimensionless vertical diffusivity is set to $K_o^* = 0.028$ and $K_o^* = \infty$ for the IOBL (red line)

3   and no-IOBL (black line) cases respectively.

4

5   **Figure A1**: Sensitivity of the ice-ocean drag coefficient C_{io} to **(a)** the surface wind speed

6   (m/s) and **(b)** the surface stress (kg/m/s^2), calculated using equation (A1). The black line

7   shows the mean value calculated from ITP-V 35 observations and the gray shadings indicate

8   the range of one standard deviation from the mean. The red line corresponds to the value

9   estimated by Cole et al. (2014) based on least-squares approximation.

10

11

12

(a) sea-ice thickness (Oct - Mar)
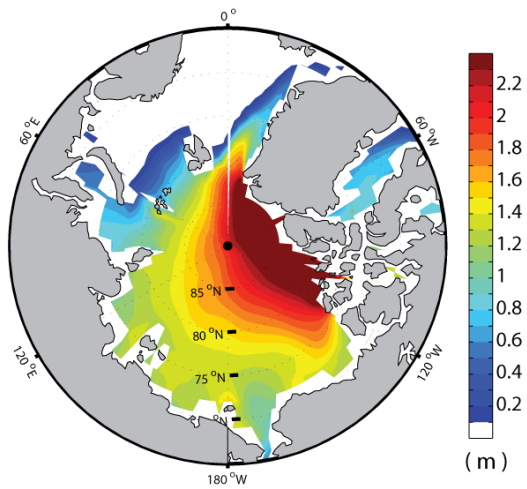
(b) sea-ice concentration (Oct - Mar)
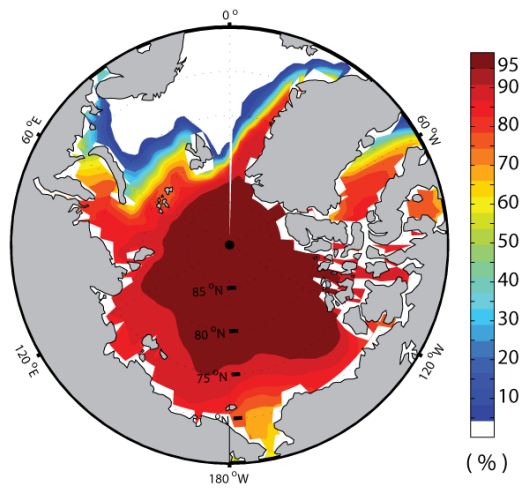
1

2

3 **Figure 1**: **(a)** sea ice thickness (m) and **(b)** sea ice concentration (%), averaged from October

4 2009 to March 2010. Sea ice thickness is from PIOMAS and sea ice concentration data is

5 from NSDIC.

6

7

8

9

10

11

12

1

sensitivity of IOBL angle to α

Legend:
- $K^* = 0.028$; $C_{io} = 0.0071$
- $K^* = 0.1$; $C_{io} = 0.0071$

Y-axis: IOBL turning angle

X-axis: $\alpha = \sqrt{2\,K^*/C_{io}}$
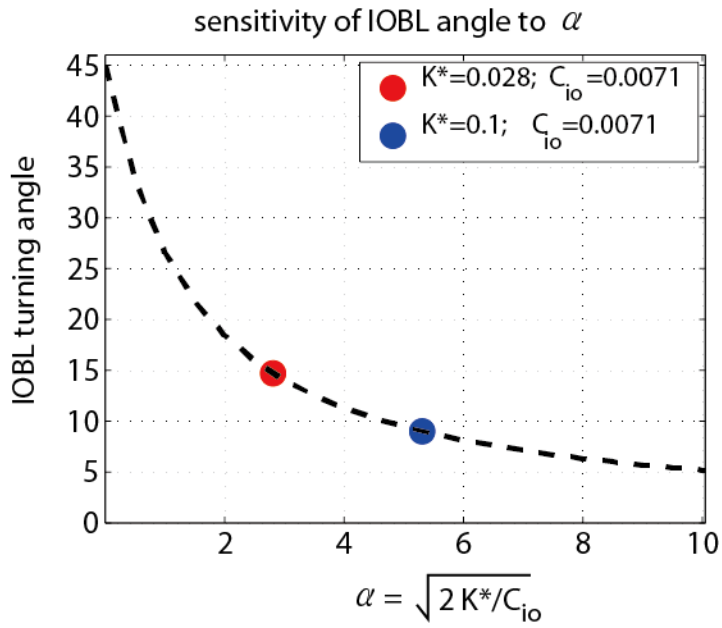
2

3

4   **Figure 2**: Sensitivity of the IOBL turning angle (θ_{IOBL}) to α $(= \sqrt{2K_0^*/C_{io}})$, calculated from

5   equation (20). The red dot corresponds to the canonical value for the vertical eddy diffusivity

6   ($K_o^* = 0.028$) and blue dot corresponds to a nominal enhanced value ($K_o^* = 0.1$).

7

8

9

10

11

12

13

14

15

16

17

18

19

20
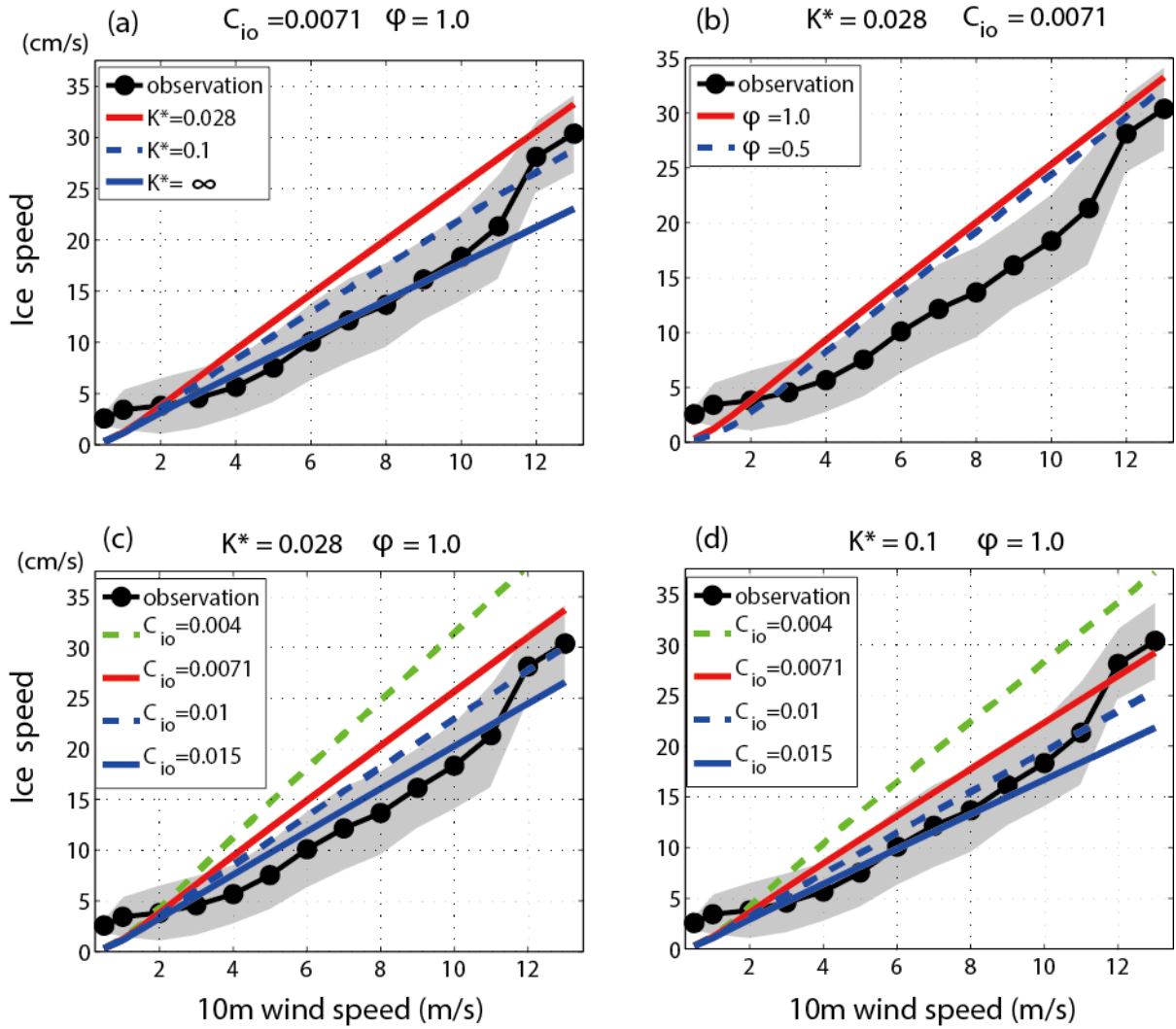
Figure 3: Sensitivity of ice speed (cm/s) to 10 m wind speed (m/s). The black line shows the mean value calculated from ITP-V 35 observations binned by 10 m wind speed, and the gray shadings indicate the range of one standard deviation from the mean. The red, dotted blue and solid blue lines correspond to our analytical model, described in Sec. 2, with **(a)** vertical diffusivities $K_o^* = 0.028, 0.1$ and ∞ (no IOBL) respectively. The sensitivity of the ice speed to the ice concentration (φ) is shown in **(b)**; the red and blue lines indicate 100 % ice cover ($\varphi = 1$) and 50% ice cover ($\varphi = 0.5$) respectively. The bottom panel shows the sensitivity of ice speed to ice-ocean drag coefficient (C_{io}), with vertical diffusivities **(c)** $K_o^* = 0.028$ and **(d)** $K_o^* = 0.1$ respectively. The bulk sea ice thickness is taken to be 1.5 m.

Wind - Ice velocity angle
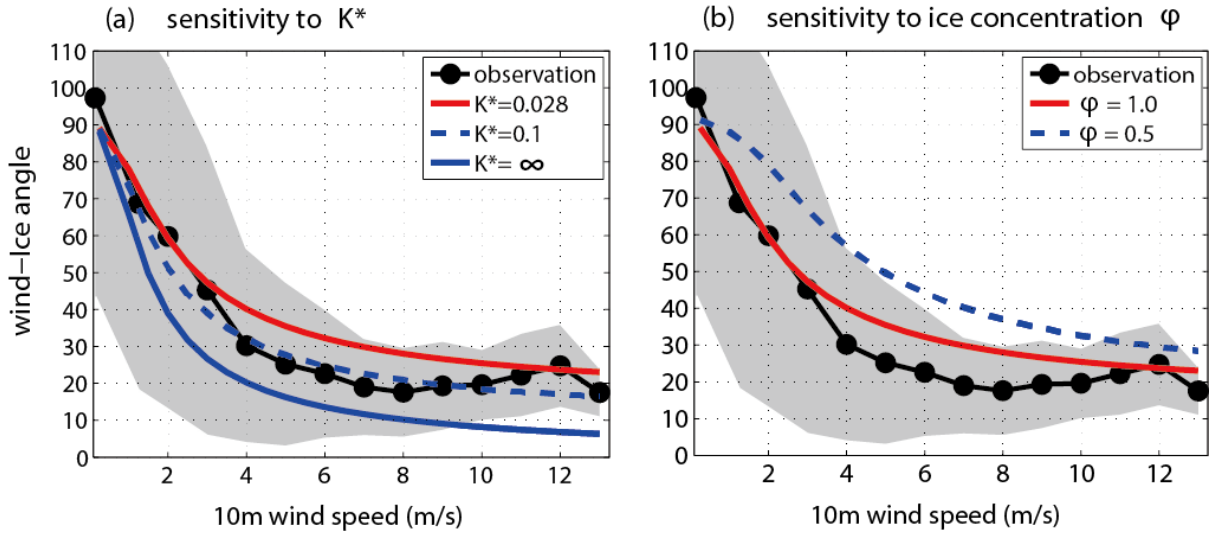
Figure 4: The velocity angle (clock-wise rotation angle) between the 10 m winds and the ITPV-35 ice floe as functions of the 10 m wind speed (m/s). Note that typically the ice velocity lies to the right of the wind velocity. In each plot the black line is mean observed value from the ITP-V 35 dataset, binned by wind speed and ice speed respectively, and the gray shadings indicate the range of one standard deviation from the mean. In **(a)**, the red, dotted blue and solid blue lines correspond to our analytical model, described in Sec. 2, with vertical diffusivities $K_o^* = 0.028$, 0.1 and ∞ (no IOBL) respectively. In **(b)**, the red and blue lines correspond to 100% ($\varphi = 1$) and 50% ($\varphi = 0.5$) sea ice concentrations, in each case using the canonical vertical diffusivity $K_o^* = 0.028$.

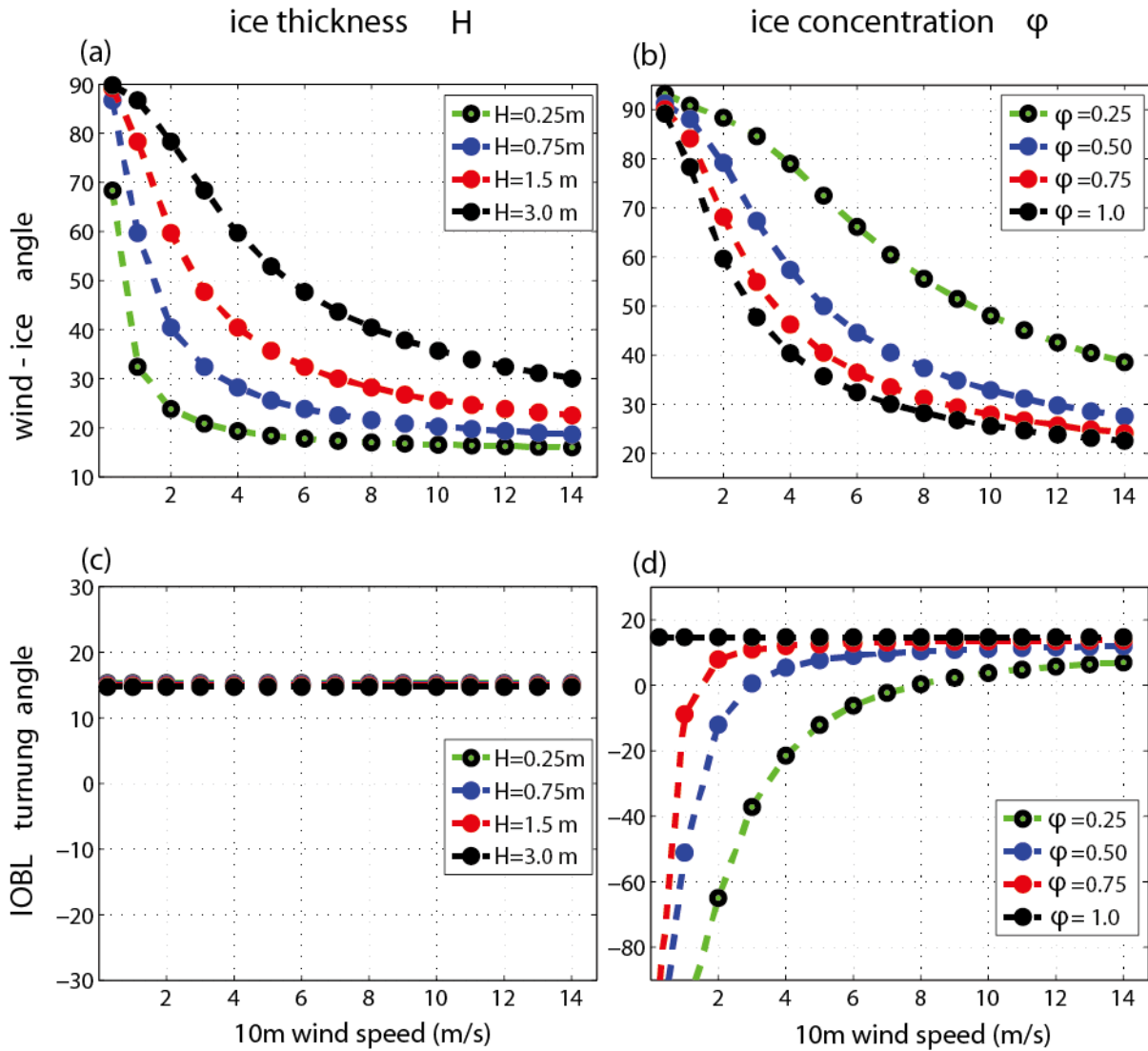**Figure 5**: The velocity angle (clock-wise rotation angle) between the ice floe and the ocean velocity at 7 m depth, as functions of the ice speed (cm/s). In each plot the black line is mean observed value from the ITP-V 35 dataset, binned by wind speed and ice speed respectively, and the gray shadings indicate the range of one standard deviation from the mean. In **(a)**, the red and blue lines correspond to our analytical model, described in Sec. 2, with vertical diffusivities $K_o^* = 0.028$ and 0.1 respectively, and using 100 % ice concentration, $\varphi = 1$. In **(b)**, the red and blue lines correspond to 100% ($\varphi = 1$) and 50% ($\varphi = 0.5$) sea ice concentrations, in each case using the canonical vertical diffusivity $K_o^* = 0.028$.

**Figure 6**: Sensitivity of **(a, b)** wind-ice velocity angle and **(c, d)** IOBL turning angle to various values of **(a, c)** sea ice thickness h_i (m) and **(b, d)** sea ice concentration (φ) as a function of 10 m wind speed (abscissa; m/s). In all panels the dimensionless vertical diffusivity is fixed at $K_o^* = 0.028$. In **(a, c)** we use 100% sea ice concentration ($\varphi = 1$), and in **(b, d)** we use a sea ice thickness of $h_i = 1.5$ m.
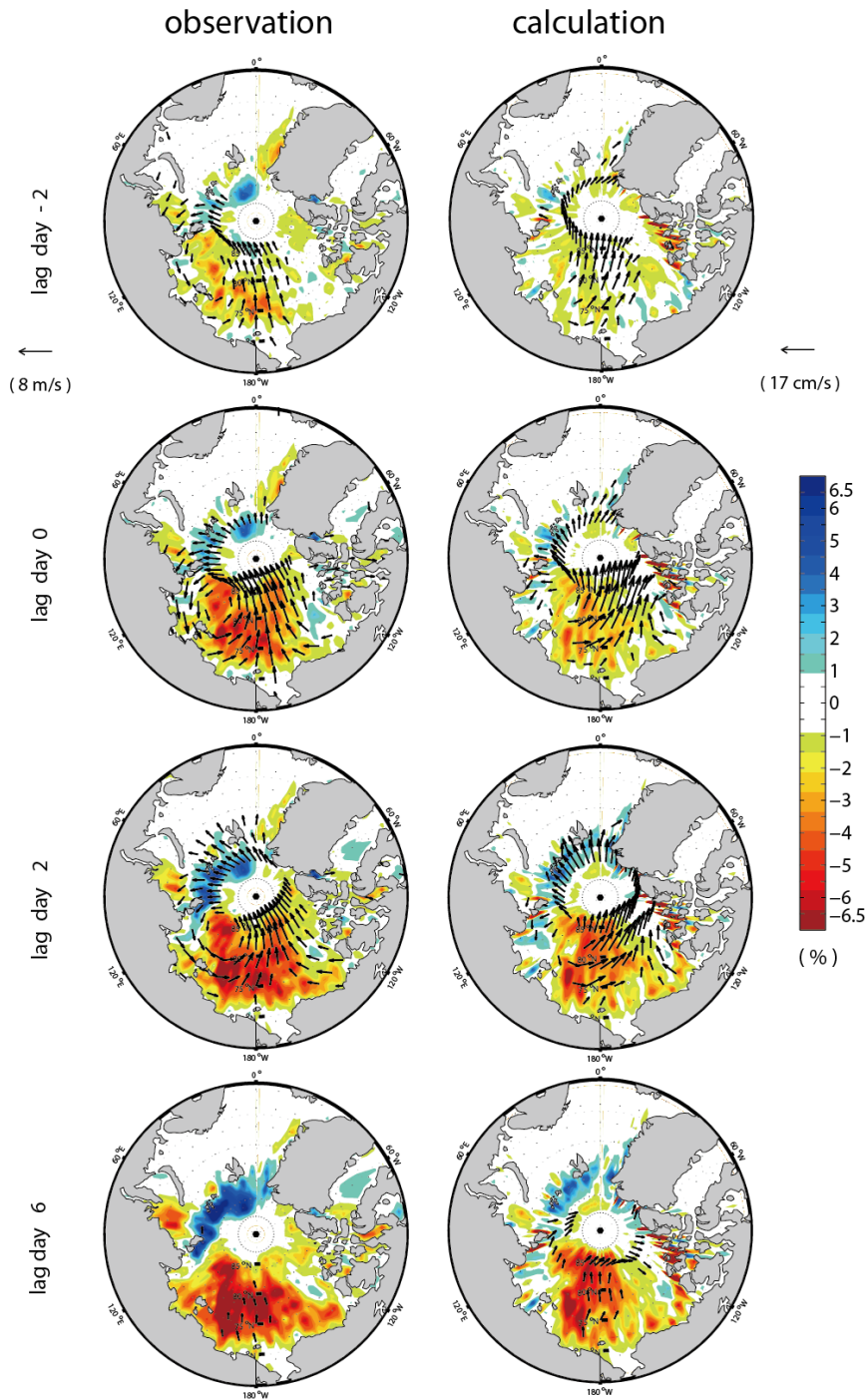
(a)   sea-ice thickness   (Aug-Sep)
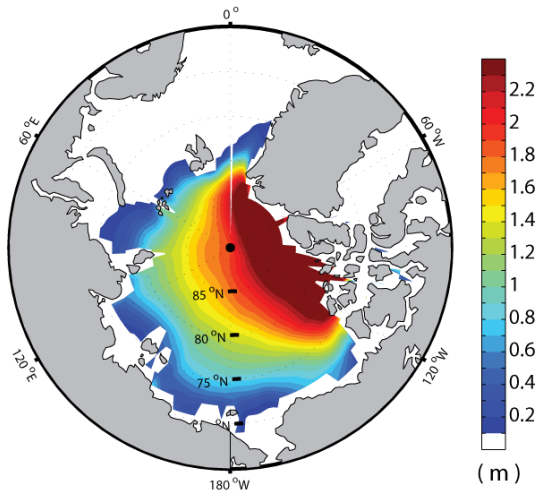
(b)   sea-ice concentration   (Aug-Sep)
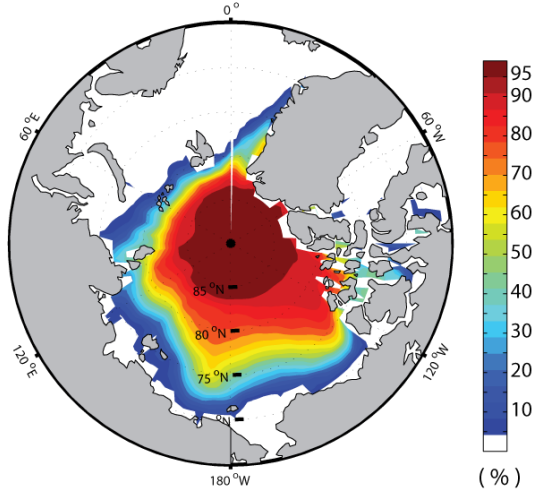
Figure 7: Aug-Sep climatological mean **(a)** sea ice thickness (m) and **(b)** sea ice concentration (%) between 1990 and 2012. Sea ice thickness is from PIOMAS and sea ice concentration data is from NSDIC.

observation   calculation

lag day - 2

lag day 0

lag day 2

lag day 6

(8 m/s)   (17 cm/s)

6.5
6
5
4
3
2
1
0
−1
−2
−3
−4
−5
−6
−6.5

(%)

1

2

3   **Figure 8**: Composites of the anomalous sea ice concentration (%) calculated from NSIDC

4   satellite observations (left column) and from our analytical model using ERA-Interim 10 m

5   wind velocity data (right column) for lag -2 days (first row), 0 days (second row), 2 day (third

6   row), and lag +6 days (fourth row). See Sec. 5 for a full description of this calculation.

7   Vectors indicate the anomalous 10m winds from reanalysis (m/s; left column) and calculated

1   sea ice velocity (cm/s; right column). For the anomalous 10m winds (left column) and sea ice

2   velocity (right column), only vectors stronger than 1.5 m/s and 3.0 cm/s are plotted
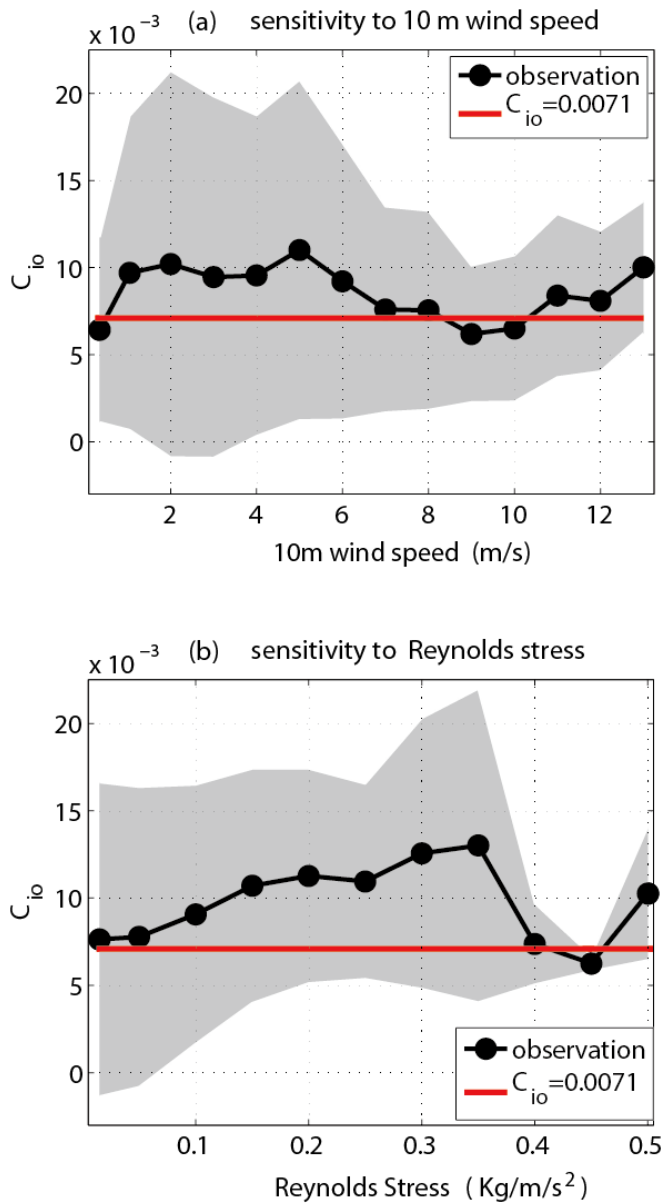
3   respectively.

4

5

6
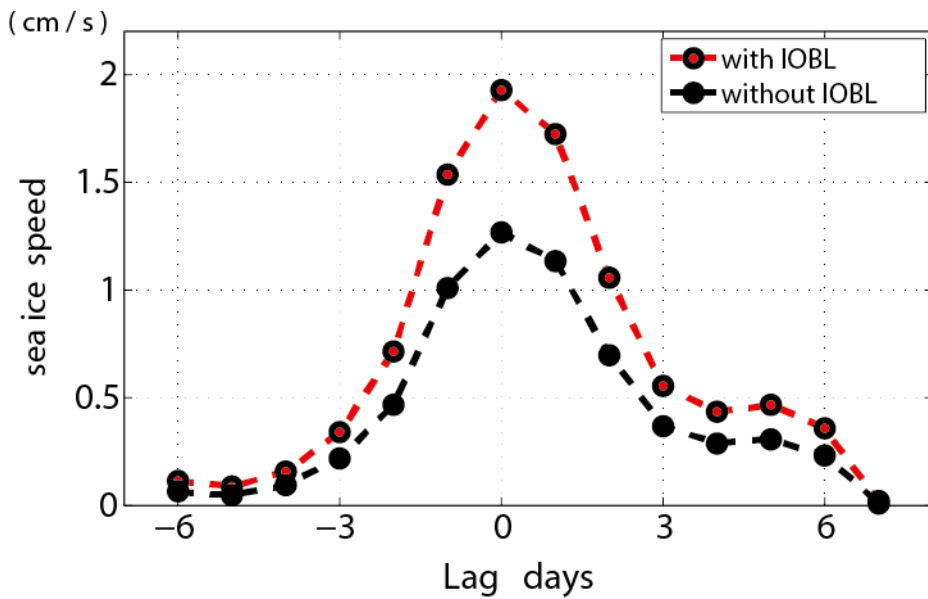
7

8

9   **Figure 9**: Lagged composite of the calculated sea ice speed (cm/s) associated with the strong

10   southerly events in the presence (red line) and in the absence (black line) of an IOBL in our

11   analytical model (in the absence of an Ekman layer the ocean surface velocity is simply set to

12   zero – the classical free drift case). The sea ice speed is area-averaged over the Pacific sector

13   of the Arctic (from 150°E to 230°E and from 70°N to 90°N). The sea ice speeds that include

14   the surface Ekman layer (red line) identical to those used to construct Fig. 8. The

15   dimensionless vertical diffusivity is set to $K_o^* = 0.028$ and $K_o^* = \infty$ for the IOBL (red line)

16   and no-IOBL (black line) cases respectively.

17

18

19

1

2

Figure A1: Sensitivity of the ice-ocean drag coefficient C_{io} to **(a)** the surface wind speed

(m/s) and **(b)** the surface stress (kg/m/s^2), calculated using equation (A1). The black line

shows the mean value calculated from ITP-V 35 observations and the gray shadings indicate

the range of one standard deviation from the mean. The red line corresponds to the value

estimated by Cole et al. (2014) based on least-squares approximation.

8